ACS APPLIED NANO MATERIALS

www.acsanm.org Article

Experimental and Numerical Investigation of Stratification Regimes in Drying Polystyrene and Silica Nanoparticle Films: Implications for Evaporative Self-Assembly of Colloidal Particles

Amanda J. Carr, Clare R. Rees-Zimmerman, Bingqian Zheng, Alexander F. Routh, and Surita R. Bhatia*

Cite This: *ACS Appl. Nano Mater.* 2024, 7, 8102−8112

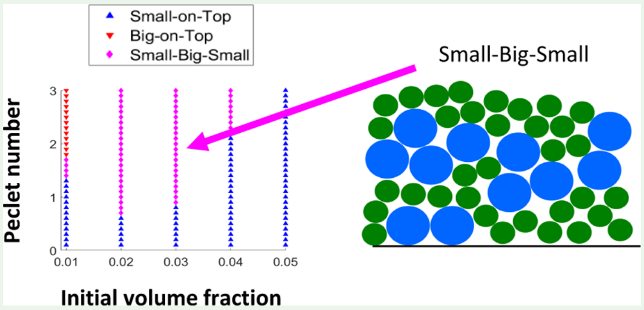

ABSTRACT: Controlled evaporative self-assembly of colloidal particles based on particle size is desirable when designing efficient, single-step deposition coating processes such as those encountered in specialized antireflective silica coatings. Particle movement during the drying process is complex. We experimentally and numerically investigate particle concentration profiles in binary colloidal films as a function of the small particle volume fraction and particle size ratio. Using a chemical potential expression that incorporates dilute interactions and also accounts for different particle size ratios, initial concentrations, and Peclet values, we calculate small and big particle concentration profiles. By characterizing the full film profile, we observe complex sandwich structures that were previously not predicted by theoretical models of film stratification and are relevant to specific coating applications. We employ microbeam X-ray scattering to characterize dried film profiles as a function of the film depth. These concentration data also show complex sandwich structures and highlight the necessity of full film characterization as opposed to only examining the surface. The presented numerical model does not correctly predict the measured film configurations, implying that additional particle interactions may need to be considered.

KEYWORDS: *stratification, colloidal films, X-ray scattering, evaporative assembly, diffusion*

INTRODUCTION

There has been a growing interest in stratification within films composed of two particle types formed through evaporative assembly. It has been observed that small particles often gather at the air−film interface. These experimental and computational results contrast with those expected by the dimensionless Peclet number, a previously determined parameter that showed good agreement with single particle-type systems and is based on a simple diffusion model.[1−4] Appropriate agreement between stratification theory and experimental results is a critical step to afford control over particle movement and subsequent stratification within solidifying films. Some examples where control is desirable include: paints and coatings with specialized properties, such as antimicrobial,[5] rust-resistant,[4] high-gloss,[4] antireflectivity,[6] and controlled hydrophobicity;[7] deposition at dissimilar interfaces encountered in flexible electronics,[8,9] energy storage devices,[10] and photonic materials;[11] inkjet printing;[12,13] and pesticide applications.[14,15]

The Peclet number (Pe) balances the rates of solvent evaporation and particle diffusion and is defined as

$$\mathrm{Pe} = \frac{6\pi\eta r H_0 \dot{E}}{k_B T} \tag{1}$$

where η is the viscosity of the solvent; r is the particle radius; H_0 is the initial film thickness; $\dot{E}$ is the speed of the receding air−solvent interface, i.e., the rate of evaporation; k_B is the Boltzmann constant; and T is the temperature.[1] In single particle size systems, Pe < 1 predicts a uniform volume fraction across the drying film. This is because particles diffuse into a homogeneous distribution faster than solvent evaporation. Alternatively, Pe > 1 predicts layering, where the moving air−film interface traps particles to form a layer, or skin, of particles. Experimental works employing NMR depth profiling,[16,17] atomic force microscopy (AFM),[17,18] cryogenic-scanning electron microscopy (SEM),[19] as well as other techniques[2,4,20] have verified these expectations.

In a system containing particles of different sizes, if Pe values of the different particles straddle unity, expansion of the simple diffusion analysis predicts that larger particles with Pe > 1

Received: February 1, 2024
Revised: March 12, 2024
Accepted: March 13, 2024
Published: April 3, 2024

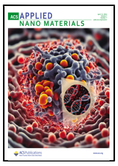

https://doi.org/10.1021/acsanm.4c00702
ACS Appl. Nano Mater. 2024, 7, 8102−8112

accumulate near the top of the film to generate big-on-top stratification. These particles will not be able to diffuse away from the moving air−solvent interface fast enough to avoid entrapment and will jam into a layer near the top of the film, while the smaller particles continue to diffuse throughout the film. The degree of stratification depends on the Pe values of both particles.[17,21,22] Samples where both Pe values are <1 should show a less stratified distribution compared to samples where both Pe values >1.[17,19,21] Maximum stratification was experimentally demonstrated in systems where the Pe values straddle unity.[17]

This type of analysis does not predict inverted, or small-on-top stratification, which has been observed computationally[22−25] and experimentally by multiple groups.[18,24−27] Evidently, factors beyond a simple diffusive analysis must also influence particle movement. For small-on-top stratification to occur, the big particle velocity away from the top of the film must exceed that of the small particles such that $U_j > U_i$ where i and j denote small and big particles, respectively. Zhou et al. computationally demonstrated small-on-top stratification by including cross terms in the chemical potential expressions.[23] They use a second virial coefficient expansion to modify the chemical potential, μ, such that ${}^{\mu_i}\!/\!{}_{k_\mathrm{B}T} = \ln(\phi_i) + 1 + \frac{2a_{ij}\phi_j}{(4/3)\pi r_j^3}$, where a_{ij} is a cross term interaction defined as $a_{ij} = {}^{2\pi}\!/\!{}_3(r_i + r_j)^3$; ϕ is the particle volume fraction; and r is the particle radius. The velocity term is $U_i \sim \frac{1}{r_i}\nabla\mu_i$, and the guiding velocity[23] condition is $\Delta U = \left(\frac{1}{\alpha}\frac{\nabla\mu_j}{\nabla\mu_i} - 1\right)U_i$ in which α is the particle size ratio, $\alpha = {}^{r_j}\!/\!{}_{r_i}$, and $\nabla\mu$ is the chemical potential gradient. Zhou et al. presented small-on-top stratification results for dilute samples with large α values as $\Delta U > 0$ in these cases. This is because of the r^3 term in virial expansion.

Fortini et al. reported[24] small-on-top stratification via computational results using a model that includes excluded volume diffusiophoresis. Fortini et al. derive $\Delta U = \left(\alpha^2\frac{K_i}{K_j} - 1\right)U_i$, where K is the sedimentation coefficient. In both the dilute and concentrated regimes, small-on-top stratification is achievable assuming ${}^{K_i}\!/\!{}_{K_j} \geq 1$ regardless of α. They qualitatively supported this argument using both simulation and experimental data with $\alpha = 7$ and large Pe values of around 100. AFM and fluorescence data showed accumulation of small particles near the top of the film. The degree of this stratification increased as the number of small particles increased. Their fluorescence data gave information about intensity against depth for the large particles, although the small particles were unlabeled. In subsequent work, both the large and small particles were fluorescently labeled, to obtain concentration profiles for both particle types.[28] Our work shows how microbeam SAXS can effectively obtain this information.

Howard et al. also utilized excluded volume diffusiophoresis and posit a condition for stratification as $\Delta U = \left(\frac{\Gamma_i}{\Gamma_j}\frac{\nabla\mu_j}{\nabla\mu_i} - 1\right)U_i$, where Γ is the effective friction coefficient.[15] Thus, the $\nabla\mu$ ratio dominates the relative particle velocity. Howard et al. computationally observed small-on-top stratification for size ratios (α) ranging from 4 to 8, and high initial small particle concentrations. Their model captured big particle "trapping" where a single layer of big particles is observed at the top of the film,[15] a feature later shown to be an artifact of the specific implicit solvent implementation.[29] Assuming a large $\frac{\nabla\mu_j}{\nabla\mu_i}$, these results match our expectations. Sear considered backflow specifically and proposed a model to consider small-on-top stratification based on the initial small particle concentration and Pe, which considered the velocity of a jammed front of small particles and the velocity of the big particles over the drying time. This inclusion of backflow reduced the strength of small-on-top stratification due to diffusiophoresis.[30]

Previously, Trueman et al. derived a continuum model for arbitrary chemical potential expressions and employed conventional colloidal hydrodynamics. They argued that the gradient in chemical potential and the particle size ratio affect particle velocity.[21] Using a chemical potential expression $\mu_i = k_\mathrm{B}T\ln(\phi_i)$, Trueman et al. computationally predicted big-on-top stratification in systems using $\alpha \sim 2$ and various geometric means of the small and big particle Pe values. However, a small-on-top configuration was not predicted but was observed experimentally.[21] Atmuri et al. used the same equations as Trueman et al. and included a surface attraction within the chemical potential equation to induce stratification, albeit without a physical basis for the surface attraction.[31]

Recently, the continuum model developed by Trueman et al. has been corrected.[32] Considering both scaling and numerical results, the diffusion-only model still predicts big-on-top stratification when μ_i includes only an entropic term. However, this model is general and allows the input of any chemical potential expressions. When excluded volume diffusiophoresis is included, accumulation of small particles at the top surface is predicted. This fluid dynamics model therefore achieves similar diffusiophoresis results as Langevin dynamics methods but through a simpler means.[15,24] There is a subtle argument concerning the degrees of freedom for the particle chemical potential expressions. This is discussed in the SI.

Notably, Cheng and Grest[33] and Sear and Warren[34] have considered stratification computationally in systems using an explicit solvent model, which may correct for overemphasis of big particle movement in implicit model works. Explicit solvent methods include backflow, which is neglected in implicit methods. However, Tang et al.[29] reported identical inverted stratification results in comparable systems computed using implicit and explicit solvents, implying that the effect of the solvent modeling approach on the stratification results may be less significant than previously thought. Continuity is ensured in our continuum modeling, and hence the inclusion or otherwise of solvent molecules is a complication for the molecular dynamics technique, rather than being fundamental to the stratification physics.

One particular challenge in studying stratification is experimental development, as many techniques are limited to sample surfaces. Liu et al. found good experimental agreement with the model proposed by Zhou et al. via AFM characterization of film surfaces using films composed of low small particle concentrations and α values between 2 and 11.[18] Similarly, Makepeace et al.[25] reported experimental and computational agreement via cryo-fractured SEM and AFM image analysis and simulation results for samples where $\alpha = 2, 7$ and $\phi_{i,0}$ varied between 0.0004 and 0.2. Their highly concentrated sample stratification results deviated from the model of Zhou et al., although this is likely because expressing the chemical potential solely through the second virial coefficient is only applicable at dilute concentrations. Small-

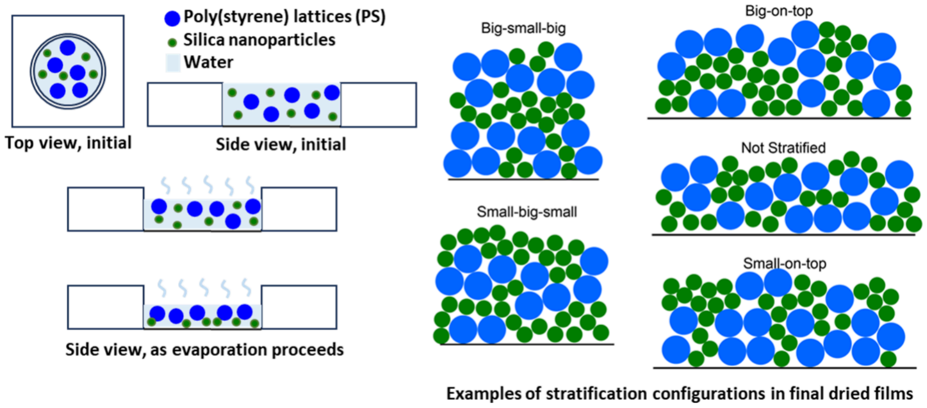

Figure 1. Schematic of the evaporative assembly process used to fabricate the films in deep-well slides in this study (left) and summary of stratification configurations (right), including complex sandwich structures where either particle type enriches both the top and bottom of a film.

angle X-ray scattering (SAXS) offers another possible experimental solution to considering different sample depths. Others have used typical[35−37] and grazing incidence[38] SAXS to consider drying colloidal films over time but lacked depth sensitivity. We previously investigated stratification within dried binary colloidal films using a microbeam SAXS technique,[26,27] focusing primarily on the effect of particle size ratio on stratification. These experiments showed complex configurations where one particle type enriches both the top and bottom of a film nonhomogeneously,[27] depicted along with other types of stratification configurations in Figure 1. This so-called sandwich structure has not, to our knowledge, been predicted by leading stratification theory but has been hinted at in computational works.[29,39]

In this paper, we investigate nonhomogenous small-on-top and complex stratification structures both numerically, using a model that includes diffusion and interaction terms within the chemical potential expression, and experimentally, using microbeam SAXS. The experiments presented here explore a different parameter space than our previous microbeam SAXS studies, focusing on the impact of the initial volume faction of small particles, $\phi_{i,0}$, rather than particle size ratio, as some theoretical studies have suggested this is an important factor in determining stratification behavior. The experimental results are thus distinct from those of previous work. The series of samples presented here does include one newly prepared sample with a similar particle size ratio, similar Pe values, and the same initial volume fraction as reported in a previous publication. This enabled us to validate our experimental approach.

Within our numerical studies, we are able to introduce any physical interaction. We choose to explore the effect of particle—particle cross terms in the description of the chemical potential via a virial expansion, as proposed by Zhou et al. We present the resulting predictions of the stratification behavior as a function of both Pe ratio and initial volume fraction. It is important to note that we are not including other interactions such as electrostatic repulsion, van der Waals attraction, or depletion. Previous diffusion-only models cannot show regimes such as the small-big-small and big-small-big sandwich structures, which have been observed experimentally. We compute particle volume fractions as a function of film depth and drying time using Zhou et al.'s chemical potential expression within a continuum model and compare these results to our experimental data. We show that complex configurations are obtainable but, perhaps unsurprisingly, find little experimental and computational agreement. This implies that the current leading models do not accurately describe our specific drying system, which would necessitate inclusion of a specific interaction. This will necessarily be more complex than Zhou et al.'s proposed first order correction.

■ EXPERIMENTAL METHODS

Numerical Analysis. A full derivation and description of the governing equations is provided elsewhere.[32] Briefly, in a system composed of two different particles, *i* and *j*, and solvent, *sol*, the particle volume average velocity, *V*, is described as

$$V_i = \frac{-1}{6\pi\eta r_i}(K_{ii}(\phi_i, \phi_j)\nabla\mu_i + \phi_j K_{ij}(\phi_i, \phi_j)\nabla\mu_j) \tag{2}$$

and likewise for component *j*. For this paper, we take *K* to be

$$K = (1 - \phi_i - \phi_j)^{6.55} \tag{3}$$

and $K_{ii} = K_{ij} = K_{ji} = K_{jj}$. This accounts for hydrodynamic hindrance as the dispersion becomes more concentrated. We define the particle chemical potentials using Zhou et al.'s equations[23] as

$$\frac{1}{k_B T}\mu_i = \ln(\phi_i) + \frac{2}{v_j}a_{ij}\phi_j + \frac{2}{v_i}a_{ii}\phi_i \tag{4}$$

$$\frac{1}{k_B T}\mu_j = \ln(\phi_j) + \frac{2}{v_i}a_{ij}\phi_i + \frac{2}{v_j}a_{jj}\phi_j \tag{5}$$

where

$$a_{ij} = \left({}^{2\pi}\!/_{3}\right)(r_i + r_j)^3 \tag{6}$$

$$a_{ii} = 4\nu_i \tag{7}$$

$$a_{jj} = 4\nu_j \tag{8}$$

and ν is the volume of the particle.

We simulate drying by using a moving, time-dependent top boundary. To enact these boundaries, we set the particle volume fraction gradients to zero at the substrate, and we set the particle fluxes $(\phi_i V_i)$ to zero at the top of the film. For a drying film with initial thickness H_0, the height of the film, *z*, is scaled via $\hat{z} = {}^{z}\!/_{H_0}$, as measured from the bottom of the film. Similarly, the drying time is scaled with the rate of evaporation $\dot{E}$ such that $\hat{t} = {}^{t\dot{E}}\!/_{H_0}$. We create a static spatial domain using $\xi = \frac{\hat{z}}{1-\hat{t}}$ to eliminate numerical difficulties associated with the moving top boundary. The drying time is transformed via $\tau = \hat{t}$. Taken together, in one dimension, the conservation equation for particle type *i* is

$$\frac{\partial \phi_i}{\partial \tau} + \frac{\xi}{1-\tau}\frac{\partial \phi_i}{\partial \xi} = \frac{1}{\mathrm{Pe}_i(1-\tau)^2}\frac{\partial}{\partial \xi}\left[\phi_i\left(K_{ii}(\phi_i, \phi_j)\frac{\partial \mu_i}{\partial \xi} + \phi_j K_{ij}(\phi_i, \phi_j)\frac{\partial \mu_j}{\partial \xi}\right)\right] \tag{9}$$

For particle type j the conservation equation is

$$\frac{\partial \phi_j}{\partial \tau} + \frac{\xi}{1-\tau}\frac{\partial \phi_j}{\partial \xi} = \frac{1}{\mathrm{Pe}_j(1-\tau)^2}\frac{\partial}{\partial \xi}\left[\phi_j\left(K_{jj}(\phi_i, \phi_j)\frac{\partial \mu_j}{\partial \xi} + \phi_i K_{ji}(\phi_i, \phi_j)\frac{\partial \mu_i}{\partial \xi}\right)\right] \tag{10}$$

The boundary conditions are no flux of particles across the top surface or the substrate.[32] The system is solved numerically using a finite volume method with Euler time-stepping. The quasi-convective term, $(\xi/(1-\tau))\,\partial\phi_i/\partial\xi$, is represented using backward finite differences for stability. An implicit assumption of this calculation is that the system is colloidally stable. We calculate the concentration of both particle types over the film height as the drying process proceeds by utilizing a time step, $\Delta\tau$, of 1×10^{-8}, and a spatial step, $\Delta\xi$, of 0.01. Stratification was determined via both particle volume fractions at the latest drying time modeled, 20% of close-packing dryness, as discussed in the Results and Discussion and Supporting Information.

Film Formation. We prepared drop-cast colloidal films using polystyrene (Invitrogen) (PS) and silica (Ludox, Sigma-Aldrich) (S) nanoparticles. As previously reported,[26] the hydrodynamic radii R_H of the PS and S were 21.4 ± 1.2 nm and 8.4 ± 1.1 nm, respectively, at their stock pH values and were measured using dynamic light scattering (NanoBrook Omni, Brookhaven Instruments). Dispersions containing 3 v/v % polystyrene particles and different concentrations of silica particles, with water as the solvent, were mixed and loaded into plastic, deep-well slides (Diatec) approximately 2.35 cm in diameter and 0.15 cm in height (Figure 1). The concentrations of silica were: 2, 3, 4, 5, and 10 v/v %. Films of each pure particle were also created. Samples were dried for about 24 h in an environmental chamber with a controlled temperature of 40.0 °C and relative humidity of 60%. Using our previously reported evaporation rate[26] value of $3.5 \times 10^{-8} \pm 3.0 \times 10^{-9}$ m/s, we calculated the Pe values via eq 1 to be 3.2 ± 0.2 and 1.3 ± 0.2 for polystyrene and silica, respectively. Final films were clear and colorless and displayed some cracks. Film thicknesses ranged from 100 to 200 μm.

Microbeam Small-Angle X-ray Scattering. Scattering data were collected on beamline 11-BM at the National Synchrotron Light Source II at the Brookhaven National Laboratory. The incident beam energy was 13.5 keV, i.e., a beam wavelength of 0.918 Å, and the beam flux was 2.2×10^9 photons/s. The full width at half-maximum beam size was 29.9 μm. Scattered and incident beam data were collected using a Dectris Pilatus 2 M detector with a pixel size of 172 μm positioned 5.130 m from the sample.

Film pieces were cut using a razor blade, while the films were within the Diatec deep-well slides, such that the film thickness in the beam direction did not exceed ~0.1 mm, to discourage excessive absorption. We then excised these cut pieces from the slides using tweezers, mounted them on glass coverslips with a minimal amount of grease, and attached the coverslips to an aluminum stage using a minimal amount of grease. Scattering data were collected under a vacuum at ambient temperature over a q range of 2.38×10^{-3} to 1.80×10^{-1} Å^{-1} starting at the top of the film. The sample stage was then translated in 10 μm steps, such that the incident beam probed different film depths (Figure 2). Data were collected for 120 s at each spot to provide good resolution. Films containing mixtures of silica and polystyrene and pure films containing only silica or polystyrene were considered. When scanning through the films, the top surface and bottom surface of the films could be identified both using the highly asymmetric patterns obtained when the beams hit the vacuum−film and film−coverslip interfaces and from the order of magnitude changes in intensity that occurred at these interfaces, when going from vacuum to the films at the top interface and then from the films to the solid glass coverslips. The scattering patterns at these interfaces were not included in the analysis. We could not adjust the tilt of the stage to account for any potential issues with poor leveling of the film, although in principle this could be done if the stage were adjustable, using the scattering patterns from the interfaces.

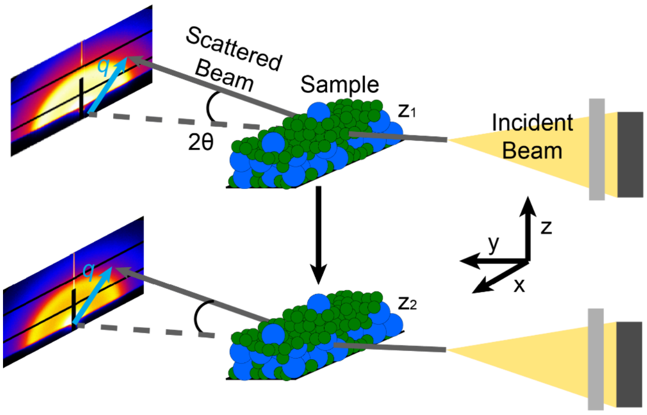

Figure 2. Schematic showing microbeam small-angle X-ray scattering setup and procedure. An X-ray source generates a beam, which is focused through various optics and clipped via shutters to obtain a small beam spot size. This incident beam travels through the sample, and both the incident beam and the one scattered at a small angle 2θ are detected. The distance between these signals is called q. The sample is translated in the positive z direction from location z_1 to a new location z_2, and the process is repeated on a new film depth.

Collected scattered data were analyzed using a linear combination analysis.[26,27] The film mixture intensity scattering data, $I_{\mathrm{PS+S}}$ are fit using pure film scattering data, I_{PS} and I_{S} for polystyrene and silica, respectively, by minimizing the normalized sum of squares to obtain coefficients a and b. In other words,

$$aI_{\mathrm{PS}}(z) + bI_{\mathrm{S}}(z) = I_{\mathrm{PS+S}}(z) \tag{11}$$

This was completed for each measured film depth. The factors a and b were normalized to the average intensity value of each pure sample and multiplied by the expected maximum volume fraction to generate local volume fractions. Equation 11 is an approximation; strictly speaking, the binary mixture will have different structure factors from the pure systems, as packing in the binary system can give rise to local configurations not present in either pure system. However, both our pure films and the binary films are disordered and do not show any signatures of long-range order; thus, we find that eq 11 gives a reasonable approximation of the total scattering. We also note that eq 11 does not account for any scattering from interstitial regions. The results presented in this paper are on dried films and were performed under vacuum; thus, we do not need to account for scattering from solvent or air between the particles. Our analysis would need to be modified for systems containing solvent.

Typical goodness of fit values, R^2, were >0.97. Uncertainty in the volume fractions derived from our fits was calculated based on R^2, and these are shown as error bars in Figure 3. In most cases, the error bars are too small to be easily seen. A large number of data points, approximately 800 values of $I(q)$, are generated at each film position and are used as inputs into the fits; thus, the resulting estimated uncertainties in the silica volume fractions are small. We attempted an alternative method of estimating the uncertainty based on the average uncertainty in I for each film position, which we estimate as $I_{\mathrm{err}} = [\mathrm{err_{shot}}^2 + \mathrm{err_{std}}^2]^{1/2}$, where $\mathrm{err_{shot}}$ is the Poisson-like shot noise error associated with photon counting statistics for a signal of a given intensity in the 1D average curve and $\mathrm{err_{std}}$ is the standard deviation of the 2D data along an arc at a particular q. However, this resulted in uncertainty estimates smaller than the uncertainty based on R^2; thus, we plotted the more conservative estimate of the uncertainty in Figure 3.

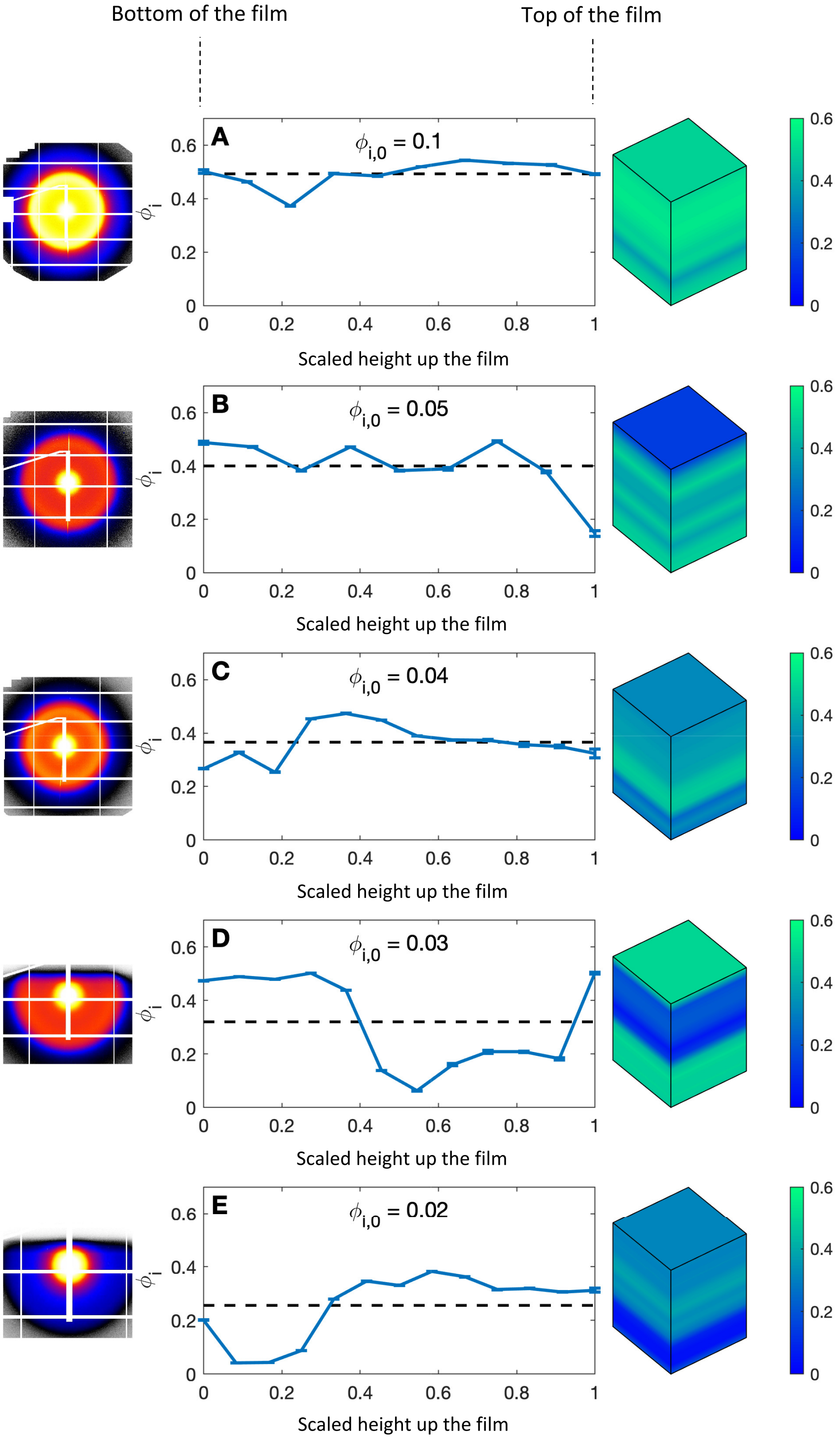

Figure 3. Experimentally determined small particle volume fraction data vs scaled height up the film, with representative small-angle X-ray scattering detector images at the center of each film (left of each plot) and three-dimensional visualizations (right of each plot) for (A) $\phi_{i,0} = 0.10$; (B) $\phi_{i,0} = 0.05$; (C) $\phi_{i,0} = 0.04$; (D) $\phi_{i,0} = 0.03$; and (E) $\phi_{i,0} = 0.02$. In all cases, $\phi_{j,0} = 0.03$, the particle size ratio $\alpha = 2.55$, and $\text{Pe}_i = 1.3$. Color bars accompanying the data visualizations scale from blue to green for the small particle volume fraction. Black dashed lines represent the expected average small particle volume fraction for each plot.

Given the relatively weak scattering of polystyrene relative to silica, only the concentration of silica is considered in this paper, although we expect that this procedure can also be applied to films composed of two particles which scatter well, assuming the structure factors of each particle within the pure film are sufficiently similar to the structure factors of each particle within the mixed film.

■ RESULTS AND DISCUSSION

We probed the small particle volume fraction as a function of film depth with microbeam SAXS. Films were prepared by using a constant amount of big particles, $\phi_{j,0} = 0.03$, and a varied amount of the small particles. We present the determined small particle volume fraction over the normalized film, representative

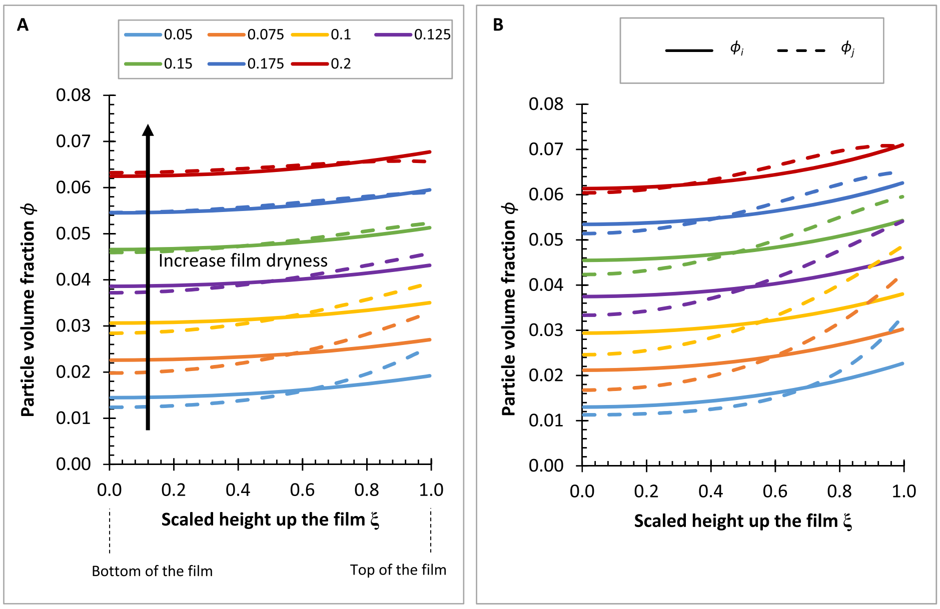

Figure 4. Calculated small (solid) and big (dashed) particle volume fractions at different dryness values, γ (colors), for (A) $\phi_{i,0} = \phi_{j,0} = 0.01$, $\text{Pe}_i = 0.9$, and $\alpha = 4$ and (B) $\phi_{i,0} = \phi_{j,0} = 0.01$, $\text{Pe}_i = 1.7$, and $\alpha = 4$, plotted over scaled height up the film ξ. Arrow shows the increase in film dryness. All dryness values are calculated via eq 12.

SAXS detector images from the middle of each film, and 3D visualizations of the concentration data in Figure 3. The black dashed lines indicate the expected average small particle volume fraction in the film, calculated based on the initial dispersions. The areas above and below this line should be equal due to particle conservation; in practice, we find they are within approximately 10% of one another.

At the highest small particle initial volume fraction, $\phi_{i,0} = 0.1$ (Figure 3A), the small particle volume fraction matches that of the expected average volume fraction across almost the entire film. We observed a dip in the small particle volume fraction near $\xi \sim 0.20$. Because our scattering analysis uses scattering data from both the big and small particles, we can reasonably assume big particles occupy vacant spaces between small particles. Thus, there are likely more big particles at this film depth. Overall, the film is homogeneous or nonstratified. When we decrease $\phi_{i,0}$ to 0.05 (Figure 3B), we observe a depletion of small particles at the top of the film. The small particle volume fraction tends to hover above the expected average from $\xi = 0$ to 0.75. At the top of the film, large particles likely dominate the scattering signal. Although there is only one datum at the top of the film supporting a lack of small particles, we characterize the sample as big-on-top because each datum represents 10 μm of film depth, and we intentionally oversample to increase the reliability of the obtained data. We suspect in these cases the particles distribute homogeneously via Brownian diffusion. Any plausible weak stratification is overpowered by the higher concentration of small particles, with respect to the big ones.

At $\phi_{i,0} = 0.04$ (Figure 3C), we see a different particle distribution. The small particle volume fraction slightly surpasses the expected average concentration, and particles congregate near $\xi = 0.3$. Toward the top of the film, the small particle volume fraction matches the expected average. At the bottom of the film, however, there are notably fewer small particles and an excess of big particles. Given the excess of small particles near $\xi = 0.3$, we classify this sample as a complex big-small-big sandwich structure. This complex stratification is highlighted in the visualization of the concentration data (Figure 3C, right).

We observe another sandwich structure for $\phi_{i,0} = 0.03$ (Figure 3D) where small particles exceed the expected average small particle volume fraction at both the bottom and top of the film to generate a small-big-small structure. In this case, $\phi_{j,0}$ is also 0.03. The presence of the sandwich structure in this sample agrees with structures observed in a separate series of samples, prepared similarly but with slightly larger small particles and slightly faster evaporation rates.[27] In the current work, we find this small-big-small sandwich for conditions of $\phi_{i,0} = 0.03$, $\phi_{j,0} = 0.03$, and particle size ratio $\alpha = 2.55$, $R_{\text{H},i} = 8.4$ nm, $R_{\text{H},j} = 21.4$ nm, $\text{Pe}_i = 1.3$, and $\text{Pe}_j = 3.2$, where R_H are the hydrodynamic radii. In our previous study,[27] we found a small-big-small sandwich under conditions of $\phi_{i,0} = 0.03$, $\phi_{j,0} = 0.03$, particle size ratio $\alpha = 2.2$, $R_{\text{H},i} = 9.9$ nm, $R_{\text{H},j} = 21.4$ nm, $\text{Pe}_i = 2.1$, and $\text{Pe}_j = 4.6$. It should also be noted that this small-big-small structure has not been observed through evaporative assembly outside of the current study and previous work from our group,[27] except in cases where there are sedimentation effects.[40,41]

As the initial small particle volume fraction decreases again to $\phi_{i,0} = 0.02$, a small-on-top structure is obtained (Figure 3E). We speculate that these complex sandwich structures occur when there is a delicate balance between the particle size ratio and initial particle volume fractions that allows an observable crossover from an entropically dominated chemical potential gradient to an interaction-dominated chemical potential gradient. The two obtained sandwich structures at $\phi_{i,0} = 0.04$ and $\phi_{i,0} = 0.03$ employ this careful balance of initial particle volume fraction and α.

We numerically considered systems with small Pe and α values and varied the starting concentration of both particles as well as Pe_i. We verified the reasonableness of these calculations by checking the mass balance for each particle type as the number of particles is conserved throughout the drying process (Figure S1). Stratification type was determined by visually inspecting both the small and big particle volume fractions at the latest computed drying time. Although our fluid model can only consider systems before close-packing, significant structural changes are unlikely to occur during late stage drying, as particle movement becomes progressively hindered.[23] We describe film dryness, γ, by taking the film concentration at the latest computed time in the drying process, τ_f, as a percentage of the close-packing fraction, ϕ_m, taken here to be 0.64. Specifically

$$\gamma = \frac{\phi_i(\tau_f) + \phi_j(\tau_f)}{\phi_m} \tag{12}$$

In our systems, the dryness value at which the model was stopped was 20%. It was checked that, for all runs, $\phi_i(\tau) + \phi_j(\tau) < 0.40$ at all times; i.e., eqs 4 and 5 for dilute solution remain reasonably valid. Significant structure changes are unlikely to occur at drying times later than 20% dryness of the close-packing dryness. At later times, a region of the film reaches close packing, and the applicability of the model ceases. As stressed, because the final film stratification is determined during early stage drying, we are comfortable in not being able to extend the model to later stage drying.[23,25] We characterize films visually by using the latest computed dryness.

Representative concentration data calculated at different times within the drying process are listed in Figure 4. Figure 4A shows a final small-on-top structure calculated using $\phi_{i,0} = \phi_{j,0} = 0.01$, $\mathrm{Pe}_i = 0.9$, and $\alpha = 4$. From $\gamma = 0{-}0.15$, big particles jam near the top of the film. From $\gamma = 0.175{-}0.2$, we observe an accumulation of small particles near the top of the film. This movement generates the final inverted or small-on-top stratification structure. A final complex sandwich structure is presented in Figure 4B, as determined using $\phi_{i,0} = \phi_{j,0} = 0.01$, $\mathrm{Pe}_i = 1.7$, and $\alpha = 4$. Again, for $\gamma = 0{-}0.175$, the big particles congregate at the top of the film. However, by $\gamma = 0.2$ (Figure 4B), we observe an increase in the small particle volume fraction at the very top of the film. While there remains a large amount of big particles near $\xi \sim 0.90$, the small particle volume fraction dominates that of the big particles at $\xi \sim 1.0$.

We calculated volume fraction values for a range of $\phi_{i,0}$ and Pe_i values using $\alpha = 2$, 4, and 6 and plot these values with their final stratification classifications (Figure 5). For our smallest size ratio, $\alpha = 2$, we see only big-on-top stratifications over all values of Pe_i and $\phi_{i,0}$. Increasing α to 4 yields different particle profiles. For $\phi_{i,0} = 0.01$, inverted small-on-top stratification occurs when $\mathrm{Pe}_i \leq 1.3$. Interestingly, for Pe_i values between 1.4 and 1.7, complex small-big-small sandwich structures appear. The largest tested size ratio, $\alpha = 6$, shows only small-on-top stratification. These data demonstrate that a diffusion model with cross terms in the interaction potential can show different stratification regimes, including complex sandwich structures.

In addition to characterizing the stratification type, we quantified the amount of stratification for the obtained concentration profiles, which is a potentially useful parameter within a variety of stratification applications. For each system, we calculated the degree of stratification (DS) for both the small and big particles using eq 13 where τ_f is the final computed drying time and i and j represent small and big particles.

$$\mathrm{DS}_i = \frac{\int_0^1 \left(\phi_i - \frac{\phi_{i,0}}{1-\tau_f}\right)^2 (1-\tau_f)\mathrm{d}\xi}{\left(\frac{\phi_{i,0}}{1-\tau_f}\right)^2}, \quad i = i, j \tag{13}$$

In a stratified system containing a layer of small particles, $\mathrm{DS}_i > 0$, as the normalized difference between ϕ_i and the expected average particle volume fraction $\frac{\phi_{i,0}}{1-\tau_f}$ is large. As DS_i approaches 0, we anticipate no small particle stratification, as the small particle volume fraction matches that of the average particle volume fraction. In this case, the small particles are homogeneously distributed. To distinguish between no stratification and big particle stratification, we define a separate degree of stratification term to consider the big particles in the system. For a system containing a stratified layer of large particles, $\mathrm{DS}_j > 0$. Similarly, a homogeneous distribution of big

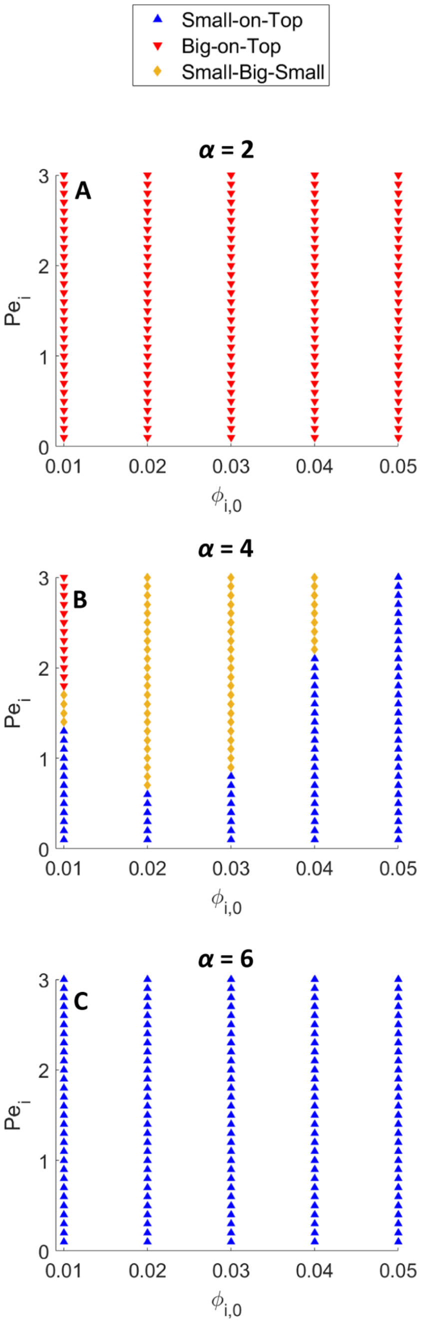

Figure 5. Final stratification configuration for samples calculated with different small particle Peclet values (Pe_i) and initial small particle volume fractions ($\phi_{i,0}$) for particle size ratios (α) of: 2 (A), 4 (B), and 6 (C). The symbols correspond to the stratification configuration, as assigned visually based on both the small and big particle volume fractions at the latest computed drying time with respect to close-packing dryness. In all cases, $\phi_{i,0} = \phi_{j,0}$.

particles yields $DS_j = 0$. Taken together, these metrics can provide characterization of both traditional and complex layering regimes, the latter of which may be misclassified by considering only one particle type. For example, a partially dried system of evenly distributed small particles with more big particles toward the top of the film differs from a system containing small particles at the bottom of the film and big particles at the top. Both of these may be characterized as big-on-top although their specific particle makeup over depth differs. Using these DS parameters though, we would expect $DS_i \sim 0$ in the first case and $DS_i > 0$ in the latter, while $DS_j > 0$ in both cases.

We plotted DS for both the small and big particles over the initial small particle volume fraction and small particle Pe number for $\alpha = 4$ (Figure 6). DS data for the remaining α values are provided in Figure S2. At $\phi_{i,0} = 0.01$ and $Pe_i \leq 1.3$, both DS_i and $DS_j \sim 0$, implying that the sample is not strongly stratified with either particle (Figure 6A, B). For $1.4 < Pe_i < 1.7$, both degrees of stratification remain close to zero, but the final film configuration changes to a small-big-small sandwich structure. Given the low stratification values, this complex stratification does not include obvious layering, and particle volume fractions tend to remain close to the average value. For $Pe_i \geq 1.7$, DS_i remains close to 0, but DS_j increases slightly, implying that the big particles are more stratified than the small ones. Given the final classification as big-on-top, we infer that the big particles jam into a distinct layer during the drying process. As the initial small particle volume fraction increases, both degrees of stratification also increase dramatically, with final DS_i and DS_j approaching 0.06 (DS_j) and 0.08 (DS_i) for all Pe_i at $\phi_{i,0} = 0.04$ and 0.05. These larger degree of stratification values imply that the sample is strongly stratified at higher Pe_i and $\phi_{i,0}$ values. Both the big and small particles distinctly congregate nonhomogeneously to yield small-on-top structures.

Evidently, complex sandwich structures are obtained only for specific initial concentrations, Pe, and size ratio values. We posit that sandwich structures form because the cross terms within the chemical potential equations become more significant at different rates for each particle as drying proceeds and the total concentration increases. At the beginning of the drying process, the entropic term, $\ln(\phi)$, dominates the chemical potential values for both small and large particles. Large particles jam near the top of the film because they cannot escape the moving air−solvent interface. As drying continues, the film concentration increases, and the cross term, $\frac{2}{v_i}a_{ij}\phi_i + \frac{2}{v_j}a_{jj}\phi_j$ for particle j, becomes sufficient such that the flux of particle j is greater than for particle i. Thus, the big particles move away from the air−solvent interface faster than the small particles, and small-on-top structures can be obtained. Systems with very low α values ($\alpha = 2$) are therefore diffusion-dominated and yield big-on-top stratification (Figure 5A). Systems with higher α values ($\alpha = 6$) are instead dominated by the cross term and show small-on-top stratification (Figure 5C). Complex sandwich structures occur when the chemical potential for the big particles crosses from diffusion-dominated to cross-term-dominated at some critical concentration during drying. Depending on the point in the drying process at which this concentration is achieved, sandwich structures may be obtained.

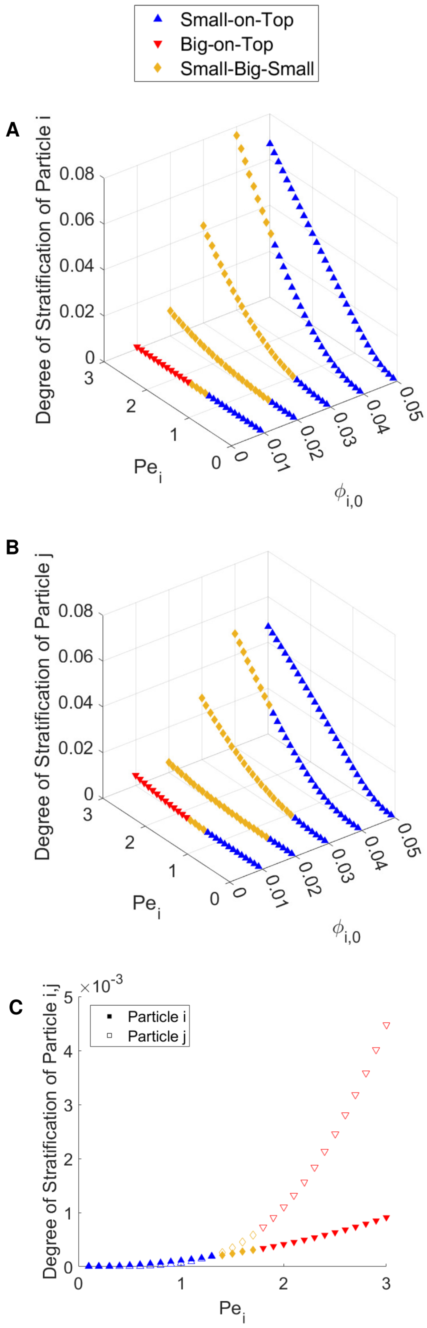

Figure 6. Degree of stratification of small particles, i, (A) and big particles, j, (B) plotted over small particle Peclet number (Pe_i) and initial small particle volume fraction ($\phi_{i,0}$) using a size ratio (α) of 4 and $\phi_{i,0} = \phi_{j,0}$. Close-up of degree of stratification (C) plotted over Pe_i for $\phi_{i,0} = 0.01$ for small particles, i, (filled markers), and big particles, j, (unfilled markers).

Lastly, we calculated the small and large particle volume fractions over the drying process for all film depths using $\alpha = 2.55$ for different Pe_i and $\phi_{i,0}$ values to mimic our experimental data. The degrees of stratification for both particles plotted over Pe_i and $\phi_{i,0}$ are shown in Figure 7. For all calculated parameters, only a big-on-top stratification is observed. $DS_i \sim 0$ and $DS_j \sim 0$ for all Pe_i values when $\phi_{i,0} = 0.01$. For $\phi_{i,0} = 0.02$, DS_i remains close to 0, while DS_j increases rapidly with Pe_i. This increase in stratification with Pe_i is as expected for these big-on-top systems in which movement is dominated by the balance of diffusion and evaporation. For the remaining concentrations examined, the degree of stratification for both the small and big particles increases with both Pe_i and $\phi_{i,0}$, other than for DS_i and DS_j having values at $\phi_{i,0} = 0.05$ that are lower than those at $\phi_{i,0} = 0.04$. This decrease in DS_i and DS_j with $\phi_{i,0}$ for larger $\phi_{i,0}$ values

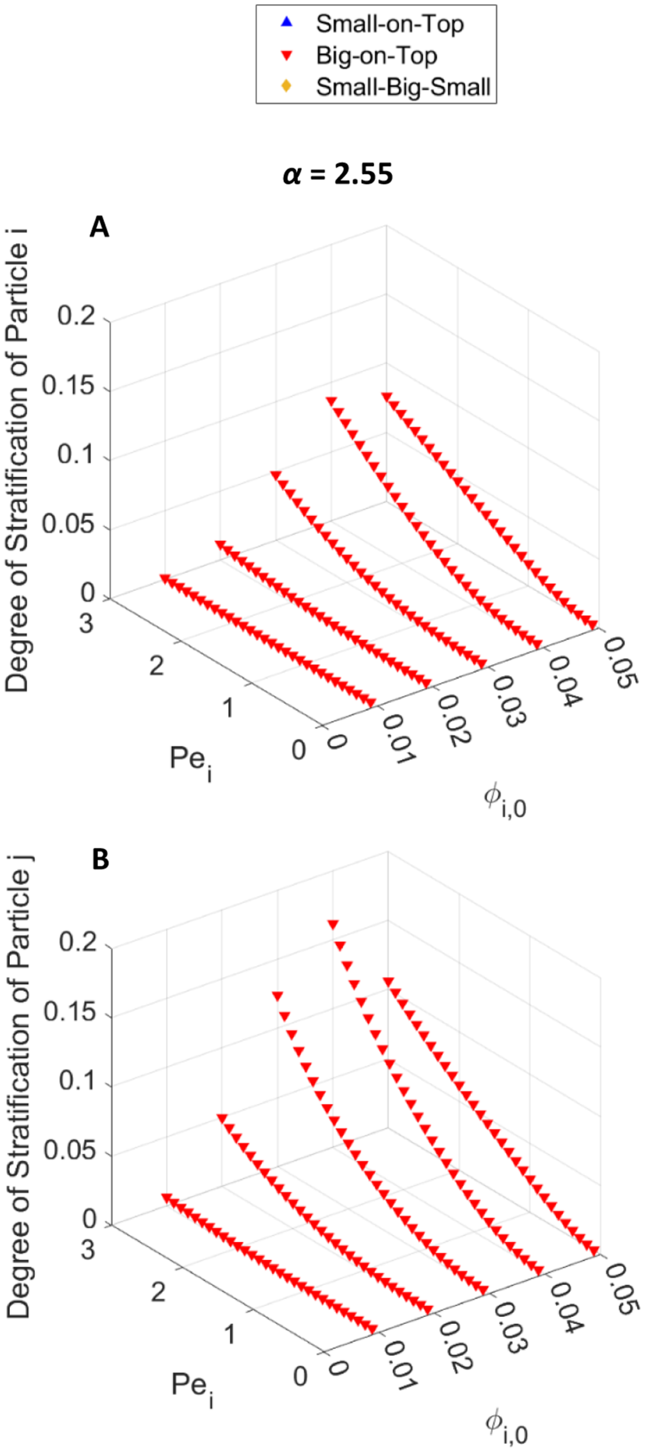

Figure 7. Degree of stratification of small particles, *i*, (A) and big particles, *j*, (B) plotted over small particle Peclet number (Pe$_i$) and initial small particle volume fraction ($\phi_{i,0}$) using a size ratio (α) of 2.55 and $\phi_{i,0} = \phi_{j,0}$.

may be due to less time for stratification to develop before γ = 20% is reached. The metric DS$_i$ approaches 0.1 and DS$_j$ approaches 0.2 for Pe$_i$ = 3 and $\phi_{i,0}$ = 0.04, meaning in these cases the samples are significantly more stratified than their low concentration counterparts. These final predicted structures agree with our experimental data only for $\phi_{i,0}$ = 0.05. All other samples do not match. Experimentally, we observe small-on-top stratification and two different complex sandwich structures, and computationally we only predict big-on-top stratification. The obvious explanation is that the chemical potential term used in the modeling is that due to Zhou et al.[23] and is not fit to our experimental system.

Evidently, the current computational approach does not fully capture the particle movement in our drying films. While our diffusion model with cross terms included within the chemical potential formulas assists in particle congregation calculations and demonstrates complex stratification regimes, the final film structures do not match our experimental data. We speculate that a different balance between the diffusion and interaction terms of the chemical potential is necessary to predict particle movement. Nonetheless, the calculated data presented may serve as a guide for future complex stratification experiments. The experimental and computational mismatch likely means that other forces present during the drying process dominate particle movement. Because our model uses an arbitrary chemical potential equation from Zhou et al.[23], one could measure and include these interaction potentials directly. The present work does not utilize excluded volume diffusiophoresis but ensures material continuity. Adding diffusiophoresis with different interaction potentials is another possible improvement.

■ CONCLUSIONS

We investigate particle stratification in films composed of two differently sized particles using both computational and experimental methods. Controllable stratification is desired in specialized film applications, such as antireflective silica coatings. Our computational model uses a diffusional approach and includes a cross term proposed by Zhou et al.[23] in the governing chemical potential expressions and approximations for the particle compressibility. For small Peclet numbers and small particle size ratios, α = 2, we calculate big-on-top stratification. At a slightly larger particle size ratio, α = 4, complex sandwich structures emerge for very dilute concentrations and midrange Peclet values where the small particles enrich both the top and bottom of the film. Larger Peclet values show big-on-top stratification, and all higher concentrations display inverted small-on-top stratification. At the largest size ratio, α = 6, all calculated data show small-on-top stratified. We speculate complex regimes form in systems where the chemical potential experiences a crossover from diffusion to interaction dominated. This change is observed only in specific cases that balance the initial particle volume fractions and size ratios. In other cases, particles are governed either entirely by diffusion, as shown for α = 2, or entirely by the interaction terms, as shown for α = 6.

Experimentally, we employ microbeam small-angle X-ray scattering to probe small particle volume fraction as a function of height up the film. As we progressively vary the initial concentration of small particles, we observe no stratification, big-on-top, small-big-small sandwich, big-small-big sandwich, and small-on-top. The calculated data under the same conditions do not match our experimental observations. Interestingly, if we consider particle volume fractions compared to the expected average volume fraction, we observe a slight agreement between the experimental and computational results. The model predicts that particles will congregate into distinct layers, which we observe. The disagreement between the modeled and experimental data highlights the necessity for accurate chemical potential expressions. The interparticle interactions within the drying system are more complex than the utilized first order correction, and control over these is needed to achieve controllable stratification in industrial films of interest.

We numerically and experimentally identify a potential regime in which complex stratification configurations may be considered. These sandwich structures highlight the importance of examining the full concentration profiles of dried films as examination of only the film surface may be misleading. Additionally, complex structures are subtle and may be mischaracterized by insufficient instrument resolution.

Our model emphasizes the relationship of obtained concentration values and the input chemical potential equations. Interestingly, we observe complex sandwich structures using simplified chemical potential expressions that modify our previous diffusional approach. Additional works probing the physical basis of the chemical potential formulas and different formulations are necessary to link calculated concentration profiles and experimental results.

■ ASSOCIATED CONTENT

Supporting Information

The Supporting Information is available free of charge at https://pubs.acs.org/doi/10.1021/acsanm.4c00702.

Computational results demonstrating conservation of mass, explanation of calculation of degree of stratification and additional results, and comments on the hydrodynamic model employed in the computations (PDF)

■ AUTHOR INFORMATION

Corresponding Author

Surita R. Bhatia − *Department of Chemistry, Stony Brook University, Stony Brook, New York 11733, United States;* orcid.org/0000-0002-5950-193X; Email: surita.bhatia@stonybrook.edu

Authors

Amanda J. Carr − *Department of Chemistry, Stony Brook University, Stony Brook, New York 11733, United States;* Present Address: Chemical Sciences and Engineering Division, Argonne National Laboratory, Lemont, IL 60439, USA; orcid.org/0000-0002-8224-7677

Clare R. Rees-Zimmerman − *Department of Chemical Engineering and Biotechnology, University of Cambridge, Cambridge CB3 0EZ, U.K.;* Present Address: Department of Chemistry, Physical and Theoretical Chemistry Laboratory, University of Oxford, Oxford OX1 1DP, UK.

Bingqian Zheng − *Department of Chemistry, Stony Brook University, Stony Brook, New York 11733, United States;* Present Address: Sonoco, Hartsville, SC 29550, USA.

Alexander F. Routh − *Department of Chemical Engineering and Biotechnology, University of Cambridge, Cambridge CB3 0EZ, U.K.;* orcid.org/0000-0002-3443-3053

Complete contact information is available at: https://pubs.acs.org/10.1021/acsanm.4c00702

Notes

The authors declare no competing financial interest.

■ ACKNOWLEDGMENTS

This research used beamline 11-BM, CMS, of the National Synchrotron Light Source II, and computing facilities of the Center for Functional Nanomaterials, a U.S. Department of Energy (DOE) Office of Science User Facility operated for the DOE Office of Science by Brookhaven National Laboratory under Contract DE-SC0012704. The authors thank Dr. Kevin Yager for his assistance with the microbeam SAXS experiments and analysis. Patrick Welche is thanked for his help with numerical schemes. Partial support for A. J. C. was provided by the National Science Foundation through awards CBET-1335787 and CBET-1903189, the Petroleum Research Fund award 55729-ND9, and a Department of Education Graduate Assistance in Areas of National Need (GAANN) fellowship Award P200A160163. C. R. R.-Z. was funded by an Oppenheimer studentship from the University of Cambridge.

■ REFERENCES

(1) Routh, A. F.; Zimmerman, W. B. Distribution of particles during solvent evaporation from films. *Chem. Eng. Sci.* **2004**, *59* (14), 2961−2968.

(2) Lee, W. P.; Gundabala, V. R.; Akpa, B. S.; Johns, M. L.; Jeynes, C.; Routh, A. F. Distribution of surfactants in latex films: A Rutherford backscattering study. *Langmuir* **2006**, *22*, 5314−5320.

(3) Routh, A. F. Drying of thin colloidal films. *Rep. Prog. Phys.* **2013**, *76* (4), No. 046603.

(4) Nikiforow, I.; Adams, J.; Konig, A. M.; Langhoff, A.; Pohl, K.; Turshatov, A.; Johannsmann, D. Self-stratification during film formation from latex blends driven by differences in collective diffusivity. *Langmuir* **2010**, *26* (16), 13162−7.

(5) Fulmer, P. A.; Wynne, J. H. Development of broad-spectrum antimicrobial latex paint surfaces employing active amphiphilic compounds. *ACS Appl. Mater. Interfaces* **2011**, *3* (8), 2878−84.

(6) Sung, Y.; Malay, R. E.; Wen, X.; Bezama, C. N.; Soman, V. V.; Huang, M. H.; Garner, S. M.; Poliks, M. D.; Klotzkin, D. Anti-reflective coating with a conductive indium tin oxide layer on flexible glass substrates. *Appl. Opt.* **2018**, *57* (9), 2202−2207.

(7) Statt, A.; Howard, M. P.; Panagiotopoulos, A. Z. Solvent quality influences surface structure of glassy polymer thin films after evaporation. *J. Chem. Phys.* **2017**, *147* (18), 184901.

(8) Tekin, E.; Smith, P. J.; Schubert, U. S. Inkjet printing as a deposition and patterning tool for polymers and inorganic particles. *Soft Matter* **2008**, *4* (4), 703−713.

(9) Zhu, J.; Hersam, M. C. Assembly and Electronic Applications of Colloidal Nanomaterials. *Adv. Mater.* **2017**, *29* (4), 1603895.

(10) Sharifi Dehsari, H.; Kumar, M.; Saad, A.; Hassanpour Amiri, M.; Yan, C.; Anwar, S.; Glasser, G.; Asadi, K. Thin-Film Polymer Nanocomposites for Multiferroic Applications. *ACS Appl. Nano Mater.* **2018**, *1* (11), 6247−6257.

(11) Wiersma, D. S. Disordered photonics. *Nat. Photonics* **2013**, *7* (3), 188−196.

(12) van Dam, D. B.; Kuerten, J. G. M. Modeling the drying of ink-jet-printed structures and experimental verification. *Langmuir* **2008**, *24*, 582−589.

(13) Huang, Y.; Li, W.; Qin, M.; Zhou, H.; Zhang, X.; Li, F.; Song, Y. Printable Functional Chips Based on Nanoparticle Assembly. *Small* **2017**, *13* (4), 1503339.

(14) Faers, M. A.; Pontzen, R. Factors influencing the association between active ingredient and adjuvant in the leaf deposit of adjuvant-containing suspoemulsion formulations. *Pest Manag Sci.* **2008**, *64* (8), 820−33.

(15) Howard, M. P.; Nikoubashman, A.; Panagiotopoulos, A. Z. Stratification Dynamics in Drying Colloidal Mixtures. *Langmuir* **2017**, *33* (15), 3685−3693.

(16) Ekanayake, P.; McDonald, P. J.; Keddie, J. L. An experimental test of the scaling prediction for the spatial distribution of water during the drying of colloidal films. *European Physical Journal Special Topics* **2009**, *166* (1), 21−27.

(17) Trueman, R. E.; Lago Domingues, E.; Emmett, S. N.; Murray, M. W.; Keddie, J. L.; Routh, A. F. Autostratification in drying colloidal dispersions: experimental investigations. *Langmuir* **2012**, *28* (7), 3420−8.

(18) Liu, X.; Liu, W.; Carr, A. J.; Santiago Vazquez, D.; Nykypanchuk, D.; Majewski, P. W.; Routh, A. F.; Bhatia, S. R. Stratification during evaporative assembly of multicomponent nanoparticle films. *J. Colloid Interface Sci.* **2018**, *515*, 70−77.

(19) Luo, H.; Cardinal, C. M.; Scriven, L. E.; Francis, L. F. Ceramic nanoparticle/monodisperse latex coatings. *Langmuir* **2008**, *24*, 5552−5561.

(20) Gundabala, V. R.; Routh, A. F.; Zimmerman, W. B. A model for surfactant distribution in latex coatings. *Langmuir* **2004**, *20*, 8721−8727.

(21) Trueman, R. E.; Lago Domingues, E.; Emmett, S. N.; Murray, M. W.; Routh, A. F. Auto-stratification in drying colloidal dispersions: a diffusive model. *J. Colloid Interface Sci.* **2012**, *377* (1), 207−12.

(22) Howard, M. P.; Nikoubashman, A.; Panagiotopoulos, A. Z. Stratification in Drying Polymer-Polymer and Colloid-Polymer Mixtures. *Langmuir* **2017**, *33* (42), 11390−11398.

(23) Zhou, J.; Jiang, Y.; Doi, M. Cross Interaction Drives Stratification in Drying Film of Binary Colloidal Mixtures. *Phys. Rev. Lett.* **2017**, *118* (10), 108002.

(24) Fortini, A.; Martin-Fabiani, I.; De La Haye, J. L.; Dugas, P. Y.; Lansalot, M.; D'Agosto, F.; Bourgeat-Lami, E.; Keddie, J. L.; Sear, R. P. Dynamic Stratification in Drying Films of Colloidal Mixtures. *Phys. Rev. Lett.* **2016**, *116* (11), 118301.

(25) Makepeace, D. K.; Fortini, A.; Markov, A.; Locatelli, P.; Lindsay, C.; Moorhouse, S.; Lind, R.; Sear, R. P.; Keddie, J. L. Stratification in binary colloidal polymer films: experiment and simulations. *Soft Matter* **2017**, *13* (39), 6969−6980.

(26) Carr, A. J.; Liu, W.; Yager, K. G.; Routh, A. F.; Bhatia, S. R. Evidence of Stratification in Binary Colloidal Films from Microbeam X-ray Scattering: Toward Optimizing the Evaporative Assembly Processes for Coatings. *ACS Appl. Nano Mater.* **2018**, *1* (8), 4211−4217.

(27) Liu, W.; Carr, A. J.; Yager, K. G.; Routh, A. F.; Bhatia, S. R. Sandwich layering in binary nanoparticle films and effect of size ratio on stratification behavior. *J. Colloid Interface Sci.* **2019**, *538*, 209−217.

(28) Martín-Fabiani, I.; Fortini, A.; Lesage de la Haye, J.; Koh, M. L.; Taylor, S. E.; Bourgeat-Lami, E.; Lansalot, M.; D'agosto, F.; Sear, R. P.; Keddie, J. L. pH-switchable stratification of colloidal coatings: surfaces "on demand. *ACS Appl. Mater. Interfaces* **2016**, *8* (50), 34755−34761.

(29) Tang, Y.; Grest, G. S.; Cheng, S. Stratification of drying particle suspensions: Comparison of implicit and explicit solvent simulations. *J. Chem. Phys.* **2019**, *150* (22), 224901.

(30) Sear, R. P. Stratification of mixtures in evaporating liquid films occurs only for a range of volume fractions of the smaller component. *J. Chem. Phys.* **2018**, *148* (13), 134909.

(31) Atmuri, A. K.; Bhatia, S. R.; Routh, A. F. Autostratification in drying colloidal dispersions: effect of particle interactions. *Langmuir* **2012**, *28* (5), 2652−8.

(32) Rees-Zimmerman, C. R.; Routh, A. F. Stratification in drying films: a diffusion-diffusiophoresis model. *J. Fluid Mech.* **2021**, *928*, A15.

(33) Cheng, S.; Grest, G. S. Molecular dynamics simulations of evaporation-induced nanoparticle assembly. *J. Chem. Phys.* **2013**, *138* (6), No. 064701.

(34) Sear, R. P.; Warren, P. B. Diffusiophoresis in nonadsorbing polymer solutions: The Asakura-Oosawa model and stratification in drying films. *Phys. Rev. E* **2017**, *96* (6−1), No. 062602.

(35) Kim, S.; Hyun, K.; Kim, Y. S.; Struth, B.; Clasen, C.; Ahn, K. H. Drying of a charge-stabilized colloidal suspension in situ monitored by vertical small-angle X-ray scattering. *Langmuir* **2013**, *29* (32), 10059−65.

(36) Kim, S.; Hyun, K.; Struth, B.; Ahn, K. H.; Clasen, C. Structural Development of Nanoparticle Dispersion during Drying in Polymer Nanocomposite Films. *Macromolecules* **2016**, *49* (23), 9068−9079.

(37) Chen, X.; Fischer, S.; Men, Y. Temperature and relative humidity dependency of film formation of polymeric latex dispersions. *Langmuir* **2011**, *27* (21), 12807−14.

(38) Perlich, J.; Schwartzkopf, M.; Körstgens, V.; Erb, D.; Risch, J. F. H.; Müller-Buschbaum, P.; Röhlsberger, R.; Roth, S. V.; Gehrke, R. Pattern formation of colloidal suspensions by dip-coating: An in situ grazing incidence X-ray scattering study. *physica status solidi (RRL) - Rapid Research Letters* **2012**, *6* (6), 253−255.

(39) Tang, Y.; Grest, G. S.; Cheng, S. Stratification in Drying Films Containing Bidisperse Mixtures of Nanoparticles. *Langmuir* **2018**, *34* (24), 7161−7170.

(40) Cardinal, C. M.; Jung, Y. D.; Ahn, K. H.; Francis, L. Drying regime maps for particulate coatings. *AIChE journal* **2010**, *56* (11), 2769−2780.

(41) Baesch, S.; Price, K.; Scharfer, P.; Francis, L.; Schabel, W. Influence of the drying conditions on the particle distribution in particle filled polymer films: Experimental validation of predictive drying regime maps. *Chemical Engineering and Processing-Process Intensification* **2018**, *123*, 138−147.